

The Modulus of Toughness of Urinary Calculi

Shyh-Jen Wang

Division of Experimental Surgery, Department of Surgery
Veterans General Hospital-Taipei, Taiwan, R.O.C.
and Institute of Biomedical Engineering,
National Yang-Ming University, No. 201 Section II,
Shih-Pai Road, Taipei 11217, Taiwan, R.O.C.
e-mail: wangsj@vghtpe.gov.tw

Ming-Chuen Yip

Department of Power Mechanical Engineering,
National Tsing Hua University, Taiwan, R.O.C.

Yen-Shen Hsu

Division of Urology, Department of Surgery,
Veterans General Hospital-Taipei, Taiwan, R.O.C.

Kun-Guo Lai

Department of Power Mechanical Engineering,
National Tsing Hua University, Taiwan, R.O.C.

Shyh-Yau Wang

University of Houston, Houston, TX

To improve the efficacy of extracorporeal shock wave lithotripsy (ESWL) treatment, it is desirable to identify the physical properties of urinary calculi could offer direct correlation with their fragilities during ESWL and thus could be used to guide treatment procedures for more effective stone fragmentation. Thirty stone specimens removed surgically were compressed by an axial testing system to measure the compressive strength and trace the stress-strain curve. Image analysis software SigmaScan (Jandel Co.) was used to calculate the area under the stress-strain curve, the modulus of toughness, for each stone. The values of compressive strength measured were similar to those reported by other researchers. The modulus of toughness of urinary calculi correlates with clinical representation of the stone fragility during

ESWL. The modulus of toughness could be an index to evaluate the physical property of urinary calculi that could be used to guide treatment procedures for more effective stone fragmentation. [DOI: 10.1115/1.1431264]

1 Introduction

The treatment of urinary stone diseases has been revolutionized since the introduction of ESWL in the early 1980s [1,2]. However, because of the differences in chemical compositions and structural features of renal calculi [3], the shock wave-stone interaction during ESWL [4], and thus the efficacy of stone fragmentation, may vary significantly.

To determine the mechanical properties of renal calculi for better understanding the efficacy of stone fragmentation during ESWL, Zhang et al. [5] used Knoop and Vickers hardness measurements to study the resisting capacity of a stone against a penetrating load. They noted no particularly higher hardness value for cystine stone among the types of stone tested. However, clinical studies often reported that cystine stones were much more difficult to fragment than other urinary stones during ESWL [6]. Furthermore, Zhang et al. [7] demonstrated the fracture toughness, based on the experimental relation between Young's modulus, Vickers hardness, indentation load and the size of indenter impression, of renal calculi correlated with the observations from clinical experience. However, the Young's modulus calculated by Zhang et al. [7] was inconsistent with the data reported [8]. The fracture toughness used to determine the mechanical properties of renal calculi seems to be limited in the research interesting.

The modulus of toughness of renal calculi is essentially the concept of energy, which was also noticed previously [5,7]. This work measured the compressive strength as well as the modulus of toughness of renal calculi. The objectives of this study are to show that the energy absorbed by a stone before fracture could relate to the stone fragility during ESWL.

2 Materials and Methods

The stones removed from patients are either in curved or polygonal shapes. Only 30 out of thousands of renal calculi, which were in bigger sizes and able to fit the test machine, were included in this study. To maximize the usage of those calculi, we decided to run the basic mechanical property (compressive) test, as Kaneko et al. [9] did, instead of fatigue test in that the fatigue properties could be related to the basic mechanical properties [10,11]. Not only the tensile strength would need much longer specimens but also the compressive strengths were reported much higher than those of tensile strengths [9]. To run the compressive test instead of the tensile test would be the cost-effective choice.

The calculi crystal compositions were determined by crystallographic analysis (Urolithiasis Laboratory, Veterans General Hospital-Taipei, Taiwan, ROC). Stones were cut into maximal rectangular solids using a low-speed diamond saw (Isomet, Buechler, IL, USA) as specimens. An axial torsion servo-hydraulic testing system (Instron Co. USA) compresses the specimens to evaluate the strength of stones. It should be noted that the

Contributed by the Bioengineering Division for publication in the JOURNAL OF BIOMECHANICAL ENGINEERING. Manuscript received by the Bioengineering Division Mar. 13, 2001; revised manuscript received Aug. 31, 2001. Associate Editor: C. H. Turner.

Table 1 Toughness modulus and material properties of renal calculi

Stone Composition	Toughness Modulus (Kpa)	Compressive Strength (Mpa)	Elasticity Modulus (Mpa)
COM	325±31	6.17±0.43	137.8±43.28
MAPH	159±20	3.79±0.31	47.84±5.46
UA	180±23	4.81±0.28	94.98±6.28
CA	164±13	3.20±0.53	28.22±2.59

Values expressed in Mean±SD

loading rate was kept in 0.05 mm/min to avoid dynamic effect. The whole testing procedure was recorded by a microprocessor to trace out the loading and displacement curves. With the loading and displacement curve, we could get the stress and strain curve by dividing the area and length, respectively.

From the stress-strain curve, the total area under the curve is called the modulus of toughness, the energy absorbed per unit volume of material when loaded to fracture. The description of the modulus of toughness in terms of mathematical is

$$T_m = \int_0^{\epsilon_f} \sigma d\epsilon,$$

where T_m , σ , ϵ , and ϵ_f are the modulus of toughness, stress, strain, and the strain at the fracture point, respectively.

To calculate the area under curve, we used software SigmaScan (Jandel Co.) to process the image analysis. Each image was first scanned, and then calibrated the scale according to the curve coordinate settings. With the help of the analysis software, we could find the maximum loading and calculate the area under the loading-displacement curve, precisely.

3 Results

Crystallographic analysis of the 30 renal calculi revealed their chemical compositions as: calcium oxalate monohydrate (COM) 9, magnesium ammonium phosphate hydrate (MAPH) 8, uric acid (UA) 6, and calcium apatite (CA) 7. Table I summarizes results for toughness modulus, compressive strength, and elasticity modulus.

4 Discussion

Our results show that the compressive strengths of calculi are similar to data developed by others [8,9]. However, the elasticity modulus (Young's modulus) of stones differs greatly between this study and other reports [7–9] due to renal calculi known to be complex in their chemical compositions and structural features [6].

The modulus of toughness varied from 159 to 325 KPa in ascending order from MAPH to CA, UA, and COM. The trend is consistent with the observation of stone fragility from clinical experience as stated by Pittomvils et al. [6] that "... calcium oxalate monohydrate [COM] ... characterized by a low stone fragility, whereas ... uric acid [UA] ... very fragile [6]." Zhong [7] also noted that "... phosphate (struvite and calcium apatite [CA]) stones are found to be easy to fragment, whereas uric acid [UA] and brushite stones are in the middle range, and calcium oxalate monohydrate [COM] and cystine stones are the most resistant types to ESWL therapy." The Kruskal-Wallis test showed that the difference between the modulus of toughness of those calculi was statistically significant. Furthermore, the Pearson correlation between clinical experience and the modulus of toughness was 0.866 ($p < 0.0001$). Using the modulus of toughness to explain the clinical experience, the r^2 is equal to 0.75 ($p < 0.0001$) with linear regression.

In summary, the modulus of toughness would be an index to evaluate the physical property of urinary calculi, which confirms the observations from clinical experience: viz. COM is much more resistant to shock-wave fragmentation than MAPH and CA stones. Therefore, the ESWL operation with higher energy density might have the greater potential to improve the efficacy of stone fragmentation during ESWL.

Acknowledgment

This work is supported in part by the VGH-NTHU Joint Research Program, (#VGH86-009-2, VTY88-P1-02, VTY89-P1-03), Medical Research Advancement Foundation in Memory of Dr. Chi-Shuen Tsou, ROC. The authors also thank Ms. H.C. Lee for assistance with the statistical analyses.

References

- [1] Chaussy, C., Schmiedt, E., and Jocham, D., 1980, "Extracorporeally Induced Destruction of Kidney Stones by Shock Waves," *Lancet*, **11**, pp. 1265–1268.
- [2] Chaussy, C., 1982, "First Clinical Experience With Extracorporeally Induced Destruction of Kidney Stones by Shock Waves," *J. Urol.* **249**, pp. 417–420.
- [3] Sutor, D. J., 1972, "Physical Aspects," *Urolithiasis*, edited by B. L. Finlayson, L. L. Hench, and L. H. Smith, National Academy of Science, Washington, DC., pp. 43–63.
- [4] Zhong, P., 1992, "Shock Wave Propagation in Renal Calculi in Extracorporeal Shock Wave Lithotripsy," Ph.D. dissertation, University of Texas at Arlington, Arlington, TX.
- [5] Zhong, P., Choung, C. J., and Goolsby, R. D., 1992, "Microhardness Measurements of Renal Calculi: Regional Differences and Effects of Microstructure," *J. Biomed. Mater. Res.*, **26**, pp. 1117–1130.
- [6] Pittomvils, G., Vandeursen, H., and Wevers, M. et al., 1994, "The Influence of Internal Stone Structure Upon the Fracture Behaviour of Urinary Calculi," *Ultrasound Med. Biol.*, **20**, pp. 803–810.
- [7] Zhong, P., Choung, C. J., and Preminger, G. M., 1993, "Characterization of Fracture Toughness of Renal Calculi Using a Microindentation Technique," *J. Mater. Sci. Lett.*, **12**, pp. 1460–1462.
- [8] Kaneko, H., Watanabe, H., and Takahashi, T. et al., 1979, "Studies on the Application of Microexplosion to Medicine and Biology, IV. Strength of Wet and Dry Urinary Calculi," *Nippon Hinyokika Gakkai Zasshi*, **70**, pp. 61–66.
- [9] Kaneko, H., Watanabe, H., and Takahashi, T. et al., 1977, "Studies on the Application of Microexplosion to Medicine and Biology, II. Strength and Composition of Urinary Calculi," *Nippon Hinyokika Gakkai Zasshi*, **68**, pp. 249–257.
- [10] Wang, Shyh-Jen, and Dixon, Marvin W., 1997, "A New Criterion for Positive Mean Stress Fatigue Design," *ASME J. Mech. Des.*, **119**, pp. 135–137.
- [11] Wang, Shyh-Jen, Dixon, M. W., and Huey, C. H. et al., 2000, "The Clemson Limit Stress Diagram for Ductile Parts Subjected to Positive Mean Fatigue Loading," *ASME J. Mech. Des.*, **122**, pp. 143–146.

On the Determination of the Angular Orientation of a Vertebra

B. C. E. Goris

Department of Biomedical Engineering, Faculty of Medical Sciences, University of Groningen, Groningen, The Netherlands

M. Kuipers

Department of Mathematics and Computing Science, University of Groningen, Groningen, The Netherlands

J. De Vries

Engineering Department, Hanzehogeschool of Groningen, Groningen, The Netherlands

D. J. Wever

Orthopaedic Department, University Hospital Groningen, Groningen, The Netherlands

G. J. Verkerke

Department of Biomechanical Engineering, Faculty of Medical Sciences, University of Groningen, Groningen, The Netherlands

A. G. Veldhuizen¹

Department of Orthopaedics, University Hospital Groningen, P. O. Box 30.001, 9700 RB Groningen, The Netherlands

In this paper we consider the spatial orientation of vertebrae. We take the view that, in determining their rotation angles from X-rays, the procedure applied by Drerup yields the most reliable empirical results, viz. the three angles through which a vertebra rotates about its own symmetry axes in a specific sequence. With a view to the further use of this information to analyze deformations or the motion of a spine we recommend that the Drerup angles be converted into the well-known Eulerian angles. How this can be done is the subject of this report. [DOI: 10.1115/1.1431265]

1 Introduction

In dealing with calculations concerning the strength and stiffness of the spine, we have made use of the well-known Eulerian angles φ , ψ , and θ (Fig. 1). They serve to define the spatial orientation of a vertebra, as is done in mechanical engineering in calculating, for example, the motion of long slender beams. Referring to Whittaker [1] and to Goldstein [2] we note that the rotation of a rigid body about some fixed point is governed by an orthogonal mapping \mathfrak{R} . With respect to some Cartesian coordinate system X , Y , and Z (Fig. 1), this mapping takes the form of a 3*3 matrix R with components R_{ij} , $i, j = 1, 2, 3$, which in our approach are functions of φ , ψ , and θ .

However, in medical circles, e.g., in orthopaedic surgery, usually one prefers the use of the rotation angles α , β , and γ , as proposed by Drerup [3] to the Euler angles. This because of the relative ease of measuring the former from radiographs. Here α , β , and γ refer to rotation angles about the principal symmetry axes X' , Y' , and Z' of a vertebra, moving with the latter (Fig. 2). It is understood that these rotations take place successively in the set order α , β , and then γ . Obviously, using α , β , and γ the components R_{ij} will be functions of these quantities.

The reasons why we prefer Euler angles in our analysis is that φ , ψ , and θ may assume finite values and that they can be applied commutatively. On the contrary, the quantities α , β , and γ have to be used successively in the above set order, unless they are infinitesimally small.

Our aim is to analyze the time-dependent deformation of a spine, starting from a given set of initial values of the underlying parameters. Usually, the latter are Drerup's angles α , β , and γ which in our approach have to be converted into the Eulerian angles φ , ψ , and θ .

How we have done this is outlined briefly in the following section. In this we shall use a fixed Cartesian coordinate system X , Y , and Z , the origin of which is chosen somewhere in the sagittal plane O , X , Z (Fig. 3).

¹To whom correspondence should be addressed.

Contributed by the Bioengineering Division for publication in the JOURNAL OF BIOMECHANICAL ENGINEERING. Manuscript received by the Bioengineering Division Mar. 13, 2001; revised manuscript received Aug. 31, 2001. Associate Editor: C. H. Turner.

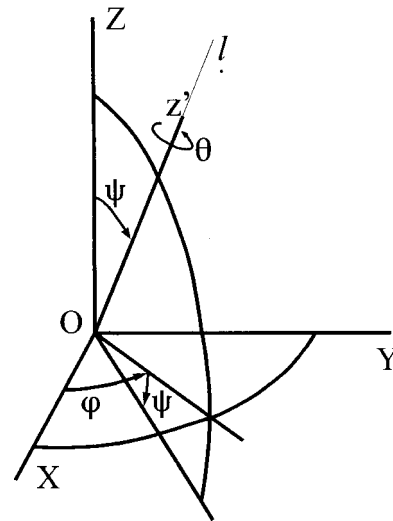


Fig. 1 The rotation of a vertebra as prescribed by the Eulerian angles φ , ψ , and θ , in which φ and ψ determine the orientation of the line l and θ the rotation about l

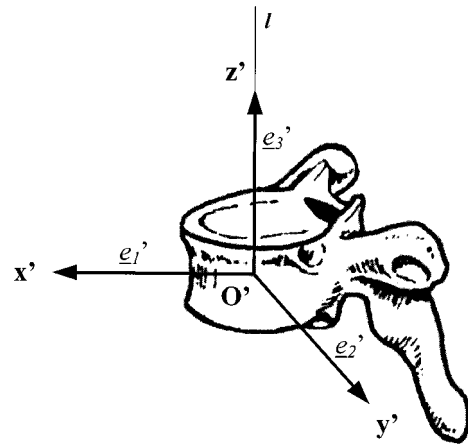


Fig. 2 The Cartesian components of the local coordinate system of the vertebra as chosen along its principal axes of inertia. The origin O' is chosen in the geometrical center of the vertebral body.

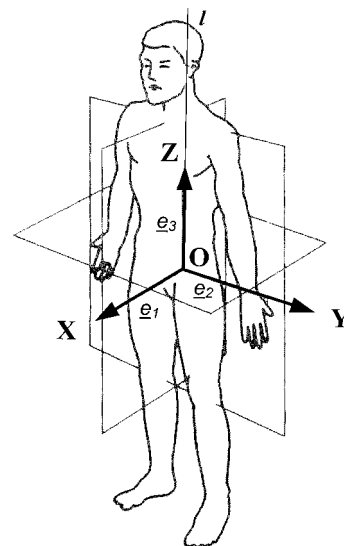


Fig. 3 The Cartesian coordinates X , Y , and Z are used as a global reference system; there is a field of uniform and constant triads of orthonormal base vectors e_i , $i = 1, 2$, and 3

2 Conversion of Generalized Coordinates

Using φ , ψ , and θ as generalized coordinates, we find

$$R[\varphi, \psi, \theta] = \begin{pmatrix} \cos \theta \cos \psi \cos \varphi - \sin \theta \sin \varphi & -\sin \theta \cos \psi \cos \varphi - \cos \theta \sin \varphi & \sin \psi \cos \varphi \\ \cos \theta \cos \psi \sin \varphi + \sin \theta \cos \varphi & -\sin \theta \cos \psi \sin \varphi + \cos \theta \cos \varphi & \sin \psi \sin \varphi \\ -\cos \theta \sin \psi & \sin \theta \sin \psi & \cos \psi \end{pmatrix}, \quad (1)$$

while in the case of α , β , and γ we arrive at

$$R[\alpha, \beta, \gamma] = \begin{pmatrix} \cos \gamma \cos \beta & -\sin \gamma \cos \beta & \sin \beta \\ \cos \gamma \sin \beta \sin \alpha + \sin \gamma \cos \alpha & -\sin \gamma \sin \beta \sin \alpha + \cos \gamma \cos \alpha & -\cos \beta \sin \alpha \\ -\cos \gamma \sin \beta \cos \alpha + \sin \gamma \sin \alpha & \sin \gamma \sin \beta \cos \alpha + \cos \gamma \sin \alpha & \cos \beta \cos \alpha \end{pmatrix}. \quad (2)$$

We note that (2) is determined empirically. Since (1) and (2) are identical, we have nine (dependent) equations for the three unknowns φ , ψ , and θ . Noting R_{ij} for the components of (2), we find

$$\psi = \arccos(R_{33}), \quad \psi \in (0, \pi), \quad (3)$$

yielding a unique value for ψ . Subsequently we see that

$$\varphi = \arccos\left(\frac{R_{13}}{\sin \psi}\right), \quad (4)$$

from which we determine two possible solutions

$$\varphi_1 \in [0, \pi] \quad \text{and} \quad \varphi_2 = 2\pi - \varphi_1 \in (\pi, 2\pi).$$

Which one applies, follows from

$$\sin \varphi \sin \psi = R_{23}. \quad (5)$$

Similarly we arrive at

$$\theta = \arccos\left(\frac{-R_{31}}{\sin \psi}\right), \quad (6)$$

yielding two possible solutions

$$\theta_1 \in [0, \pi] \quad \text{and} \quad \theta_2 = 2\pi - \theta_1 \in (\pi, 2\pi).$$

Then the choice is made through the use of

$$\sin \psi \sin \theta = R_{32}. \quad (7)$$

Table 1 Numerical results obtained from conversion of rotations about co-rotating axis to Eulerian angles

Rotation About Co-rotating Axes			Eulerian Angles		
α	β	γ	φ	ψ	θ
30 deg	0 deg	0 deg	270 deg	30 deg	90 deg
30 deg	0 deg	30 deg	270 deg	30 deg	120 deg
10 deg	-10 deg	0 deg	224.6 deg	14.1 deg	134.6 deg
10 deg	-10 deg	10 deg	224.6 deg	14.1 deg	144.6 deg
15 deg	-15 deg	0 deg	224 deg	21.1 deg	134 deg
15 deg	-15 deg	20 deg	224 deg	21.1 deg	154 deg
0 deg	-30 deg	0 deg	180 deg	30 deg	180 deg
0 deg	-30 deg	30 deg	180 deg	30 deg	210 deg
30 deg	-30 deg	0 deg	220.9 deg	41.4 deg	130.9 deg
30 deg	-30 deg	30 deg	220.9 deg	41.4 deg	160.9 deg
30 deg	-40 deg	20 deg	210.8 deg	48.8 deg	158.1 deg

A final verification follows by substituting the calculated values of φ , ψ , and θ into the remaining components of (1).

3 Numerical Results

We have applied the conversion numerically to combinations of rotations α , β , and γ , borrowed from Skalli et al. [4]. The results are shown in Table 1.

References

- [1] Drerup, B., 1984, "Principles of Measurement of Vertebral Rotation From Frontal Projections of the Pedicles," *J. Biomechanics*, **17**, pp. 923–935.
- [2] Goldstein, H., 1959, *Classical Mechanics*, Addison-Wesley, Reading, PA.
- [3] Skalli, W., Lavaste, F., and Descrimes, J., 1995, "Quantification of Three-Dimensional Vertebral Rotations in Scoliosis: What are the True Values?" *Spine*, **20**, pp. 546–550.
- [4] Whittaker, E. T., 1961, *A Treatise on the Analytical Dynamics of Particles and Rigid Bodies*, Cambridge University Press, Cambridge.

Fitting Manifold Surfaces to Three-Dimensional Point Clouds

Cindy M. Grimm¹

Computer Science Department, Washington University,
St. Louis, MO 63130

e-mail: cmg@cs.wustl.edu

Joseph J. Crisco²

Department of Orthopaedics,
Brown University School of Medicine,
Providence, RI 02912

e-mail: Joseph_Crisco@Brown.edu

David H. Laidlaw³

Computer Science Department, Brown University,
Providence, RI 02912

e-mail: dhl@cs.brown.edu

We present a technique for fitting a smooth, locally parameterized surface model (called the manifold surface model) to unevenly scattered data describing an anatomical structure. These data are acquired from medical imaging modalities such as CT scans or MRI. The manifold surface is useful for problems which require analyzable or parametric surfaces fitted to data acquired from surfaces of arbitrary topology (e.g., entire bones). This surface modeling work is part of a larger project to model and analyze skeletal joints, in particular the complex of small bones within the wrist and hand. To demonstrate the suitability of this model we fit to several different bones in the hand, and to the same bone from multiple people. [DOI: 10.1115/1.1431266]

Introduction

Digital anatomical structures extracted from medical images are finding a wide range of scientific and clinical applications ranging from finite element modeling to visualization to computer assisted surgery. An important aspect of this is the extraction of surface models of anatomical structures. Our work was stimulated in part by the need to study *in vivo* skeletal joint mechanics. We use these extracted surfaces to quantify joint kinematics, ligament strains, and distances between joint surfaces in normal, pathological, and surgically reconstructed joints [1–3]. Quantifying these effects requires a surface model which is smooth, locally parameterized, and capable of modeling surfaces of arbitrary topology.

The manifold surface model [4] meets these requirements. First, manifolds are locally parameterized, with the parameterization, and corresponding degrees-of-freedom, under the control of the user. Therefore, it is a simple matter to provide more degrees-of-freedom in areas of higher curvature. Second, the fitting process is hierarchically layered, i.e., there is a natural method for doing a coarser to finer fit; the finest fit level is local and is only performed where there is sufficient data to do so. These two properties help with interpolating sparse data since the coarser fit can be used in areas with few sample points and the finer fit applied only where needed. Manifolds are capable of modeling surfaces of arbitrary topology, so we can model entire bones, including those with topological holes and boundaries caused by incomplete data. Finally, the surface is C^k for any desired k , which results in smooth distance-to-surface calculations.

Previous Work

There are many techniques for scattered data interpolation; for a recent survey see [5]. We focus here on those which can handle arbitrary topological surfaces of C^1 (or higher) continuity: Spline surfaces [6–9], algebraic surfaces [10], subdivision surfaces [11–13], and radial basis functions or thin-plate splines [14]. Of these, all but [8], [9], [13], and [14] require a polyhedron to fit to and produce a single patch per face. It is not clear how well these techniques will work for unevenly scattered points since they provide no mechanism for smoothing or filling holes in the data. They also produce a large number of patches.

The techniques of Eck [8], Hoppe [13], and Krishnamurthy [9] produce approximating surfaces, the first two by simplifying the mesh to produce a coarse network, the last one by having the user draw patch boundaries. These approaches are closest to ours in spirit; the major difference lies in the structure of the output surface. We produce the same local parameterization, in a topological sense, for a single bone across multiple people. Spline patch tech-

niques must also fit both to the interior control points and maintain constraints across boundaries between patches, a notoriously difficult problem with unevenly distributed data.

In [14] the techniques of radial basis functions are extended to handle arbitrary topology. This approach provides smoothing and can handle unevenly scattered data; however, the topology of the final surface is not guaranteed to be the same as the input data.

Several approaches specific to modeling joint surfaces exist, such as Boyd's thin-plate splines [15] and Ateshian's B-splines [16], further developed in [17]. These techniques focus on modeling just a single contact region of the bone (topologically a plane). The dynamics of multiple joint surfaces on a single bone make a model of the entire bone (topologically a sphere) more useful than a model of just the contact region for one neighboring bone. Sherrer in [18] produces a collection of patches with enforced C^1 continuity across boundaries. They provide a complete model but only C^1 continuity and also have some difficulties enforcing boundary constraints.

Input Data and Surface Type

The data sets are outer cortical bone surfaces extracted from sequential slices of a CT image volume. The segmentation procedures involved thresholding, image algebra, and user interaction to define each bone contour [1]. This produces dense (≈ 0.01 mm) samples along widely spaced (1 mm) cross sections.

The manifold surface is described fully in [4]. The topology and rough geometry are specified by a *generator polyhedron*, which specifies the topology and an initial approximate geometry for the higher resolution *manifold polyhedron*, which in turn specifies the connectivity and an initial geometry for a set of overlapping, glued-together spline patches (see Fig. 1). The generator polyhedron is constructed by the user and can be any general polyhedron. Each level provides more degrees-of-freedom than its predecessor.

We use a different embedding equation than the one described in the paper. Our embedding is simpler and also pulls the division by the sum out of the individual patch equations. Each chart is embedded using a single NUBS [19] spline patch E_c and the result blended together using the original blend functions [4].

$$E(p) = \sum_c B_c(p) E_c(M(\alpha_c(p)))$$

where M is either the identity function (vertex and face charts) or the linear transform that takes the domain of the edge chart to the unit square (see Appendix A of [4]). The patch domains for the face charts extend beyond the chart's domain. The control points are placed on the subdivision surfaces as originally described.

The Fitting Process

The manifold is fit to the data in three steps (see Fig. 1). We assume that the user has already constructed a generator polyhedron that has the same topology shape as the data and approximately the same geometry. This takes about an hour and the resulting generator polyhedron can be used for all bones of the same type (e.g., all hamate bones have the same generator polyhedron). The fitting process brings the approximate geometry into alignment with the data points; it does not change the topology of the manifold surface.

We first find the best fit for the generator polyhedron with default positions for the manifold polyhedron vertices and spline patches. The second step adjusts the vertices of the manifold polyhedron while using the default spline patch locations. Finally, the control points of the spline patches are adjusted if there are sufficient data points that project to that patch's region of influence. Because the surface is approximately correct after fitting the manifold polyhedron, we do not need to fit patches in regions containing few or no samples. Also, we do not have to apply

¹Supported by NSF grant CCR-992009.

²Supported in part by NIH grant AR44005.

³Supported by NSF grant CCR-0093238.

Contributed by the Bioengineering Division for publication in the JOURNAL OF BIOMECHANICAL ENGINEERING. Manuscript received by the Bioengineering Division Mar. 13, 2001; revised manuscript received August 31, 2001. Associate Editor: C. H. Turner.

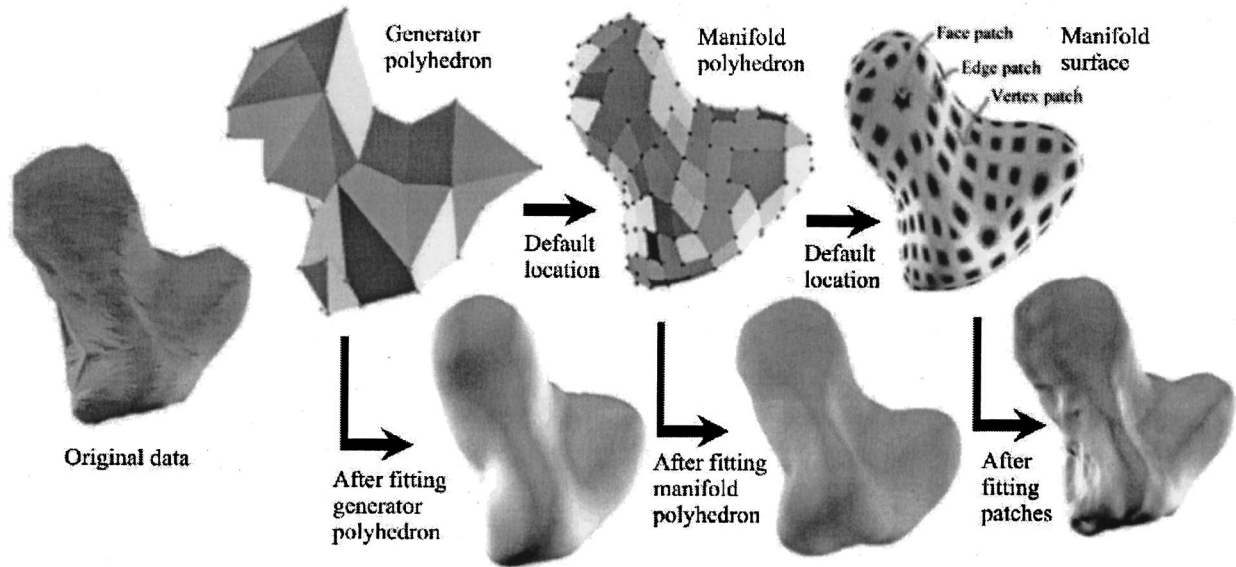


Fig. 1 From left to right top: the original data, shown triangulated. The generator polyhedron, the manifold polyhedron, and the prototype manifold surface, showing the local parameterization. Bottom: after fitting the generator polyhedron. After fitting the manifold polyhedron. After fitting the individual patches.

additional constraints to make the boundaries of the patches behave because the patches are overlapped, so boundaries of the patches do not affect the final geometry.

The Fitting Mechanism. In general, fitting can be expressed as the solution to the following minimization problem, where S is the surface and the d_r are the data points we fit to.

$$\min \left[\left(\sum_r \min_t (d_r - S(t))^2 \right) + \alpha_c E_c \right] \quad (1)$$

A point on the surface is described by $S(t)$ for some parameter value t . This equation minimizes the distance between every data point and its closest point on the surface. Additional constraints (the E_c) can be added to enforce “smooth” surfaces, i.e., ones which do not undulate unduly between the given points. The constant α_c expresses the importance of fitting the data versus producing a smooth surface. The curvature term E_c has two purposes. First, it filters noisy data. Second, if the data is very nonuniformly sampled, it serves as a guide for the behavior of the surface in very sparse areas.

Equation (1) requires a nonlinear solver. However, if the surface is reasonably well aligned with the data we can form a similar, linear expression by projecting the data points onto the surface and minimizing the resulting equations. By reasonably well aligned we mean that the closest point on the surface defines a bijection between the surface and the data points with no folds.

The linear expression is as follows:

$$\min \left(\sum_r (d_r - S(t_r))^2 \right) \quad (2)$$

where $S(t_r)$ is the point on the surface closest to d_r . A given point of S can be expressed as $S(p) = \sum_i x_i a_i(t)$ where the x_i are either the polyhedra vertices or the spline control points and the $a_i(t)$ are the blend functions, which, for a given t , evaluate to a constant. After some manipulation, minimizing S reduces to a set of linear equations with the x_i as variables. Specifically, each data point d_r produces an equation of the form $\sum_i x_i a_i^r(t_r) = d_r$, which constrains the surface at t_r to pass through the point d_r for each data point.

The linear optimization problem can be written as a solution to the matrix equation $Ax = d$, where $A = \{a_i^r(t_r)\}$, $x = \{x_i\}$ is the

vector of variable and each row r of A corresponds to a linear constraint on x imposed by the data point d_r . We solve for x using a standard least-squares solver for a linear system [20].

Note that the linear approximation, Eq. (2), differs from Eq. (1) in that we minimize the distance to a specific parameter point t on the surface, not to any point on the surface. We therefore may not find the globally optimal solution.

It remains to show how to calculate the a_i for a specific parameter point t . We begin at the patch level and work up to the generator polyhedron level. The degrees-of-freedom (the x_i s) will be different at each level, and hence so will the matrix A . At the patch level the x_i are the control points of all of the patches. An individual spline patch P_k is of the form $P_k(p) = \sum_i b_i(p) g_i^k$. The entire collection of the control points is therefore $\{g_i^k\}$. Our surface is constructed by “gluing” these individual patches together, i.e.,

$$S(t) = \sum_k \beta_k(t) P_k(t) = \sum_k \beta_k(t) \sum_i b_i(t) g_i^k(t) \quad (3)$$

where the β_k are the blend functions, one for each patch. The blend functions have the property that $\sum_k \beta_k(t) = 1$, with at most three functions nonzero.

Instead of solving for all of the degrees-of-freedom at once, producing a large but sparse matrix, we take advantage of the overlapping structure and fit patches individually. One way to ensure that $S(t_r) = d_r$ is to ensure that, for every overlapping patch P_k , $P_k(t_r) = d_r$. The resulting error will be at worst the maxi-

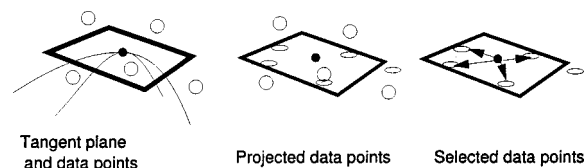


Fig. 2 Finding the four data points to interpolate between for an additional patch constraint. Left: the surface point, the tangent plane, and the nearby data points. Middle: the projected data points. Right: the selected points, shown in the tangent plane.

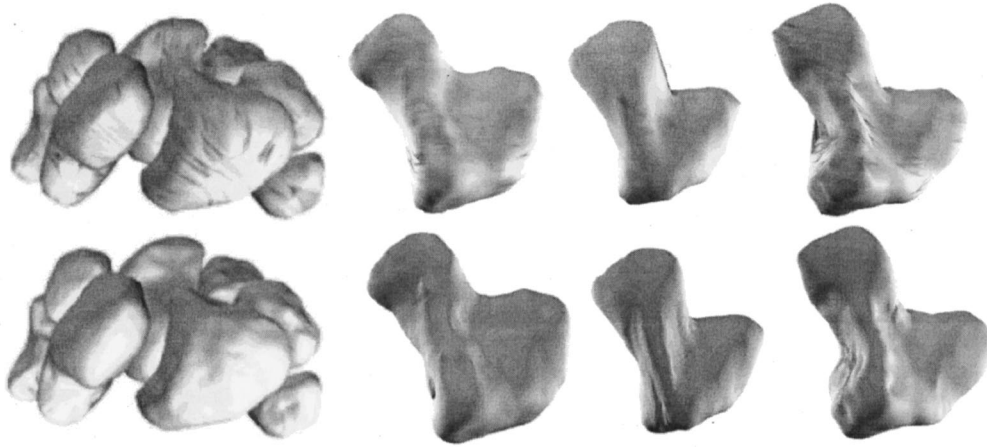


Fig. 3 The carpal bones from one person and three hamates from different people. Top: meshes produced from the data points using Nuages [22]. Bottom: manifold surfaces. Note the striation in the Nuages meshes where the slicing planes become parallel to the surface.

sum of the individual patch area, since the final surface is a linear combination of the given points. For each patch we find those data points that project onto the domain of that patch and fit to just those points.

For the manifold polyhedron, our degrees-of-freedom are the vertices of the polyhedron. Each control point g_i^k in its default location is expressed as a linear combination of the vertices of the manifold polyhedron, V_j , i.e., $g_i^k = \sum_j B_j^k V_j$. Each point on the surface is therefore of the form

$$S(p) = \sum_k \beta_k(p) P_k(p) = \sum_k \beta_k(p) \sum_i b_i(p) \sum_j B_j^k V_j. \quad (4)$$

Similarly, we can express each vertex of the manifold polyhedron, in its default location, as the sum of the vertices of the generator polyhedron.

Curvature Constraints. An advantage of the least-squares formulation is that it does a good job of approximating noisy data. Also, as demonstrated, the spline fitting problem can easily be approximated as a linear problem [21]. The least-squares formulation does, however, behave badly when the weights on a variable are close to zero (visually, this produces “spiking” in the surface). We address this problem by adding additional constraints (the E_c), which ensure that every variable has sufficient weight. When parameter α_c from Eq. (1) is set to one, then the constraint has equal weight to moving a data point an equivalent distance from the surface.

Polyhedral Constraints. When fitting the generator polyhedron and manifold polyhedron we add in additional constraints that require vertices to lie at the centroid of their neighbors. If $\{v_i\} \subset \{v_k\}$ are the n manifold polyhedron vertices forming the star of v (i.e., all the adjacent vertices) we add the constraint $\beta(v - (1/n) \sum_i v_i) = 0$.

Additional Patch Constraints. When fitting the patches we add in additional constraints at regularly spaced intervals in the parameter space, resulting in a more even support.

We take a uniformly distributed set of points in the domain (a 5 by 5 grid of points) and determine where the embedded points should go based on nearby sample points. Each new constraint finds four data points which surround the embedded point, if any exist, and interpolates between those four data points to produce the desired location for the new constraint.

To find the four surrounding data points we first project all of the nearby data points onto the tangent plane at the constraint point (see Fig. 2). Second, we find the four closest points (mea-

suring distance in the plane) such that the four points are “around” the constraint point, i.e., the normalized dot products of the projected points are bigger than 0.5. We then take the weighted average of those point’s locations.

Results

For Fig. 3 we used one person’s scan in the neutral position and the hamate bone from three subjects. We compare our models to meshes created using Nuages [22] software. The sample points we used are the vertices of the Nuages’ meshes; we did not use the Nuages’ surface connectivity information. The models ranged in size from 921 to 4754 points. The data points were spaced approximately 0.01 mm apart along the contours, with 1 mm spacing between the contours. On average, the average distance from the data points to the manifold surface is 0.053 mm with a ± 0.02 95 percent confidence interval. The average maximum distance was 0.42.

The parameter α_c produces similar results over a wide range of values (from 0.5 to 1.5) except for a few bones with spurious data points on the inside of the bones. For these bones, the larger value of α_c was required.

Discussion

One drawback of the least-squares fitting technique is that it uses the closest point to choose the parameter point; if the initial surface and the data points are misaligned this can cause folding or pinching of the surface. This problem is most obvious when the data set has two parallel surfaces close together. One solution is to adjust the generator polyhedron, but this is not very satisfactory.

Conclusion

We have demonstrated a hierarchical technique for fitting a smooth surface to an entire bone. Manifold surfaces have several desirable properties, such as smoothness and arbitrary topology, which make them useful for *in vivo*, multiple joint analysis. The technique requires a minor amount of user interaction for each new bone type, but the remainder of the process is completely automatic. The fitting process is robust in the presence of noise and unevenly sampled data points.

References

- [1] Cirsco, J. J., McGovern, R., and Wolfe, S., 1999, “A Non-invasive Technique for Measuring *in Vivo* Three-Dimensional Carpal Bone Kinematics,” *J. Orthop. Res.*, **17**, No. 1, pp. 96–100.
- [2] Cirsco, J. J., and Neu, C., 2000, “*In Vivo* Scaphoid, Lunate and Capitate Kinematics in Flexion-Extension,” *J. Hand Surg.*, **25A**, No. 5, pp. 860–869.

- [3] Pike, S., Hulsizer-Galvin, D., Weiss, A., Akelman, E., and Wolfe, S., 2001, "Carpal Flexion/Extension Kinematics are Abnormal in Both Wrists of Patients With Unilateral Scaphoid-Lunate Ligament Tears," *47th Annual Meeting, Orthopaedic Research Society*.
- [4] Grimm, C., and Hughes, J., 1995, "Modeling Surfaces of Arbitrary Topology Using Manifolds," *Comput. Graph.*, **29**, Proceedings of SIGGRAPH '95, July.
- [5] Lodha, S. K., and Franke, R., 1999, "Scattered Data Techniques for Surfaces," *Scientific visualization (Proc. Dagstuhl)*, pp. 181–222.
- [6] Peters, J., 1995, "C¹ Surface Splines," *SIAM (Soc. Ind. Appl. Math.) J. Numer. Anal.*, **32**, No. 2, pp. 645–666.
- [7] Loop, C., 1994, "Smooth Spline Surfaces Over Irregular Meshes," *Proceedings of SIGGRAPH '94*, Orlando, FL, July, pp. 303–310.
- [8] Eck, M., and Hoppe, H., 1996, "Automatic Reconstruction of B-Spline Surfaces of Arbitrary Topological Type," *Proceedings of SIGGRAPH '96*, New Orleans, LA, Aug., pp. 325–334.
- [9] Krishnamurthy, V., and Levoy, M., 1996, "Fitting Smooth Surfaces to Dense Polygon Meshes," *Proceedings of SIGGRAPH '96*, New Orleans, LA, Aug., pp. 313–324.
- [10] Bajaj, C., Ihm, I., and Warren, J., 1993, "Higher-Order Interpolation and Least-Squares Approximation Using Implicit Algebraic Surfaces," *ACM Trans. Graphics*, **12**, No. 4, pp. 327–347.
- [11] Halstead, M., Kass, M., and DeRose, T., 1993, "Efficient, Fair Interpolation Using Catmull-Clark Surfaces," *Proceedings of SIGGRAPH '93*, Anaheim, CA, Aug., pp. 35–44.
- [12] Zorin, D., Schröder, P., and Sweldens, W., 1996, "Interpolating Subdivision for Meshes With Arbitrary Topology," *Proceedings of SIGGRAPH '96*, New Orleans, LA, Aug., pp. 189–192.
- [13] Hoppe, H., DeRose, T., Duchamp, T., Halstead, M., Jin, H., McDonald, J., Schweitzer, J., and Stuetzle, W., 1994, "Piecewise Smooth Surface Reconstruction," *Proceedings of SIGGRAPH '94*, Orlando, FL, July, pp. 295–302.
- [14] Turk, G., and O'Brien, J., 1999, "Shape Transformation Using Variational Implicit Functions," *Comput. Graph.*, **33**, No. 2, pp. 335–342.
- [15] Boyd, S. K., Lenore, J., Lichti, D. D., Salkauskas, K., and Chapman, M. A., 1999, "Joint Surface Modelling With Thin-Plate Splines," *ASME J. Biomech. Eng.*, **121**, No. 5, pp. 525–532.
- [16] Ateshian, G. A., 1993, "A Least-Squares B-Spline Surface-Fitting Method for Articular Surfaces of Diarthrodial Joints," *ASME J. Biomech. Eng.*, **115**, pp. 366–373.
- [17] Ateshian, G. A., 1995, "Generating Trimmed B-spline Models of Articular Cartilage Layers From Unordered 3D Surface Data Points," *Proc. ASME Bioengineering Conference*, ASME, New York, pp. 217–218.
- [18] Scherrer, P. K., and Hillberry, B., 1979, "Piece-Wise Mathematical Representation of Articular Surfaces," *J. Biomech.*, **12**, pp. 301–311.
- [19] Bartels, R., Beatty, J., and Barsky, B., 1987, *An Introduction to Splines for Use in Computer Graphics and Geometric Modeling*, 1st Ed., Morgan Kaufmann, San Mateo, CA.
- [20] NAG, 1993, *NAG Fortran Library*, Numerical Algorithms Group, Downers Grove, IL.
- [21] Fowler, B., and Bartels, R. H., 1991, "Constraint Based Curve Manipulation," *Siggraph Course Notes 25*, July.
- [22] Geiger, B., "Nuages Reconstruction Package," *INRIA*.